EES Catalysis

ROYAL SOCIETY OF CHEMISTRY

PAPER

View Article Online
View Journal | View Issue

Check for updates

Cite this: *EES Catal.*, 2024, 2, 638

Crystal facet engineering of spinel $NiCo_2O_4$ with enhanced activity and water resistance for tuneable catalytic methane oxidation†

Yash Boyjoo,[abc] Yonggang Jin,*[a] Xin Mao,[d] Guangyu Zhao,[a] Thomas Gengenbach,[e] Aijun Du,[d] Hua Guo*[a] and Jian Liu*[bf]

Received 20th November 2023,
Accepted 25th December 2023

DOI: 10.1039/d3ey00281k

rsc.li/eescatalysis

Spinel $NiCo_2O_4$ are excellent catalysts for complete methane oxidation. Nevertheless, the spinel structure is thermally unstable and its activity is negatively affected by humidity. Herein, we report crystal facet engineering synthesis of spinel $NiCo_2O_4$ hexagonal nanosheets with different exposed facets. Density functional theory (DFT) simulations predict that a more viable reaction mechanism for methane oxidation occurs on 112-$NiCo_2O_4$ with {112} exposed facets compared with 111-$NiCo_2O_4$ with {111} exposed facets. Detailed material characterization and catalytic oxidation testing verified the DFT results showing that 112-$NiCo_2O_4$ has better thermal stability as well as higher catalytic activity towards methane oxidation than 111-$NiCo_2O_4$. Conversely, 111-$NiCo_2O_4$ has the enhanced water resistance of the two catalysts. DFT calculations suggest that OH groups tend to preferentially adsorb onto metal sites, which (1) reduces the number of active sites available and (2) makes CH_4 adsorption and activation a more arduous process. This study offers insights on the behavior of spinel oxide catalysts towards methane combustion in dry and humid conditions, further demonstrating that crystal facet engineering can be a practical strategy to tune the activity and water resistance of metal-oxide catalysts.

Broader context

Catalytic oxidation is ideal for the treatment of low concentration effluents. In this context, spinel $NiCo_2O_4$ have been found to be excellent catalysts for complete CH_4 oxidation. Nevertheless, the spinel structure is thermally unstable and its activity is negatively affected by humidity. Herein, we report crystal facet engineering synthesis of spinel $NiCo_2O_4$ hexagonal nanosheets with different exposed facets. Experimental and density functional theory (DFT) studies show that 112-$NiCo_2O_4$ with {112} exposed facets has better thermal stability as well as higher catalytic activity towards methane oxidation than 111-$NiCo_2O_4$ with {111} exposed facets. Conversely, 111-$NiCo_2O_4$ has the enhanced water resistance of the two catalysts. Modelling studies suggest that OH groups tend to preferentially adsorb onto metal sites. Nevertheless it may be possible that in humid conditions, CH_4 oxidation follows an alternative pathway on 111-$NiCo_2O_4$. This study offers insights on the behavior of spinel oxide catalysts towards CH_4 combustion in dry and humid conditions, further demonstrating that crystal facet engineering can be a practical strategy to tune the activity and water resistance of metal-oxide catalysts. These low-cost and high-performance catalysts are highly demanded for mitigating fugitive CH_4 emissions in resources and energy sectors such as coal mining, natural gas industry, natural gas engines, *etc.*

Introduction

Approximately 70% of the methane (CH_4) emitted from coal mines is released as ventilation air methane (VAM).[1] Being a much more potent greenhouse gas than CO_2,[1] efficient remediation pathways are required to be considered for the removal of CH_4 from VAM. Since thermal oxidation of dilute methane in the ventilation air requires reaction temperatures usually above 1000 °C, catalytic oxidation of lean CH_4 has been investigated extensively as a promising way to lower this temperature *via* the use of a catalytic process.[2] Catalytic oxidation is ideal for the treatment of low concentration effluents and has been successfully used for the treatment of CH_4[3–5] but also for the combustion of

---

[a] *CSIRO Mineral Resources, 1 Technology Court, Pullenvale, QLD 4069, Australia. E-mail: yonggang.jin@csiro.au, hua.guo@csiro.au*
[b] *State Key Laboratory of Catalysis, Dalian Institute of Chemical Physics, Chinese Academy of Sciences, 457 Zhongshan Road, Dalian 116023, China. E-mail: jian.liu@surrey.ac.uk*
[c] *Curtin Mauritius, Telfair, Moka, Mauritius*
[d] *School of Chemistry, Physics and Mechanical Engineering, Queensland University of Technology, Brisbane, QLD 4001, Australia*
[e] *CSIRO Manufacturing, Bayview Avenue, Clayton, VIC 3168, Australia*
[f] *DICP-Surrey Joint Centre for Future Materials, Department of Chemical and Process Engineering and Advanced Technology Institute, University of Surrey, Guildford, Surrey, GU2 7XH, UK*

† Electronic supplementary information (ESI) available. See DOI: **https://doi.org/10.1039/d3ey00281k**

other hydrocarbons such as carbon monoxide,[6] formaldehyde,[7] toluene,[8,9] propane[10] and chlorinated volatile organic compounds (VOCs).[11]

It is generally agreed that CH_4 total oxidation proceeds through a Mars–Van Krevelen (M–vK) mechanism, during which the hydrocarbon molecules get adsorbed on the metal active sites followed by stepwise oxidation using lattice oxygen.[2] The oxygen vacancies created as a result can be filled by adsorption and dissociation of oxygen from the air during reaction. While supported PdO_x nanoparticles are the state-of-the-art catalytic materials for CH_4 complete oxidation,[12] non-noble metal oxides such as Co_3O_4 hexagonal nanosheets,[13,14] Co_3O_4 nanoparticles,[5,15] Co_3O_4 nanotubes,[16] CuO nanobelts,[17] bowtie-shaped spinel $NiCo_2O_4$ catalysts,[18] and composites such as Co_3O_4/CeO_2,[19] MnO_x–NiO[20] and NiO/CeO_2[21] have also proved to be appealing candidates, with the added benefit of being much cheaper than noble metal catalysts. Spinel Co_3O_4 or $NiCo_2O_4$ type materials are among the most attractive as they can deliver complete CH_4 oxidation at temperatures in the neighbourhood of 500 °C. This is attributed to the spinel structure that allows the formation of oxygen vacancies rather easily, due to the uneven metal–oxygen bond lengths within the material's matrix. Nevertheless, the main issue with the spinel structure is that it is thermally unstable and decomposes at elevated temperatures into a much less active material.[22] For example, NiO tends to segregate from the spinel $NiCo_2O_4$ structure at elevated temperatures,[22,23] which deactivates the catalyst.

PdO_x and metal oxides nanoparticles are generally deactivated by the presence of water vapour that is normally present in dilute methane emissions.[12,24,25] This is because water molecules tend to compete for active sites or facilitate the coalescence of PdO_x nanoparticles. Consequently, the development of efficient, active and water-resistant catalysts presents a major challenge in this current field of research. Some of the strategies that have been used so far for metal oxides are compositing with other metal oxides[25] or, in the case of PdO_x, the use of supports or the addition of Pt as a promoter.[12]

Crystal facet engineering (CFE) of nanocrystals strategy has been widely reported for the enhanced catalytic activity of catalysts *via* the design and creation of specific exposed crystal planes on its surface. The unique atomic arrangements that occur as a consequence of CFE allows the possibility to stabilise high index crystal planes that can: expose abundant unsaturated active sites to adsorb and activate reactants, facilitate formation of oxygen vacancies and create structural defects such as steps and edges.[26] Over the past decade or so, CFE has been successfully applied in batteries,[27,28] gas-sensing,[29] water-splitting,[30,31] photocatalysis,[32] CO_2 conversion[33,34] and oxygen reduction/evolution reactions (ORR/OER).[35,36] Notably, CFE has been successfully applied to the catalytic oxidation of hydrocarbons. High energy surface facets in MnO_2 catalysts could facilitate the creation of oxygen vacancies compared with the low-index facets such as {110} or {100}, resulting in enhanced activities for VOC oxidation.[7,8] The exposed crystal facet {112} in Co_3O_4 was found to be responsible for its higher activity during the combustion of methane when compared with the {001} and {011} planes.[13] Unsurprisingly, the same exposed facet on Co_3O_4 hexagonal nanosheets was active for CO and toluene oxidation due to the stabilisation of oxygen vacancies, which allows the unhampered removal and replenishment of lattice oxygen during reaction.[14] Oxygen vacancies created during CFE have also shown good ability to trap metal cations within the lattice[37] and favours single-atom doping[38] for applications in catalytic oxidation reactions. CFE can be relatively easily achieved through modifying synthesis procedures (*e.g.*, use of different capping agents, solvent ratios and hydrothermal synthesis temperatures) and is therefore an attractive and straightforward approach to be employed to tune the catalytic properties of crystal surfaces.

Herein, we applied CFE to synthesise two $NiCo_2O_4$ catalysts with similar morphologies and textural parameters but with different exposed crystal facets. As a result, we created 111-$NiCo_2O_4$ and 112-$NiCo_2O_4$ having a hexagonal nanoplate morphology and with {111} and {112} exposed crystal facets, respectively. Combined experimental and theoretical studies were performed to investigate the effect of the exposed crystal facets on the materials' catalytic activities and stabilities for CH_4 oxidation reaction under both dry and humid conditions. We found that the high index {112} exposed facet afforded better activity and stability to $NiCo_2O_4$ hexagonal nanosheets while the {111} facet offered enhanced water resistance. Through theoretical calculations, we then acquired fundamental understandings on how the presence of water vapour in the feed decreases the catalysts' activities. The impressive stability of 112-$NiCo_2O_4$ is demonstrated through long-term stability testing under humid conditions for 230 h reaction time. This study offers some insights into the behaviour of different exposed facets of spinel $NiCo_2O_4$ for CH_4 catalytic oxidation under dry and humid conditions. It also shows that CFE can be a useful strategy to tune the activity and water resistance of metal-oxide materials by offering alternative reaction pathways in catalytic oxidation reactions for the treatment of lean effluents.

Results and discussion

Characterization

The procedure for the synthesis of 111-$NiCo_2O_4$ and 112-$NiCo_2O_4$ is given in the ESI.† The X-ray diffraction (XRD) patterns of the 111-$NiCo_2O_4$ and 112-$NiCo_2O_4$ samples calcined at different temperatures are shown in Fig. S1 and S2 (ESI†), respectively. Both 111-$NiCo_2O_4$ and 112-$NiCo_2O_4$ samples exhibit spinel $NiCo_2O_4$ structure at 400 °C calcination temperature. However, the spinel structure of 111-$NiCo_2O_4$ decomposes to show obvious NiO peaks (at $2\theta = 51°$ and $74°$) at a calcination temperature of 450 °C while these peaks appear in 112-$NiCo_2O_4$ at a higher calcination temperature of 500 °C. The spinel structure is made up of AO_4 and BO_6 tetrahedral and octahedral cells, respectively, where A and B are metal atoms. When Ni atoms are doped into the spinel structure, they tend to occupy the octahedral sites of $NiCo_2O_4$.[39,40] Due to the difference in the

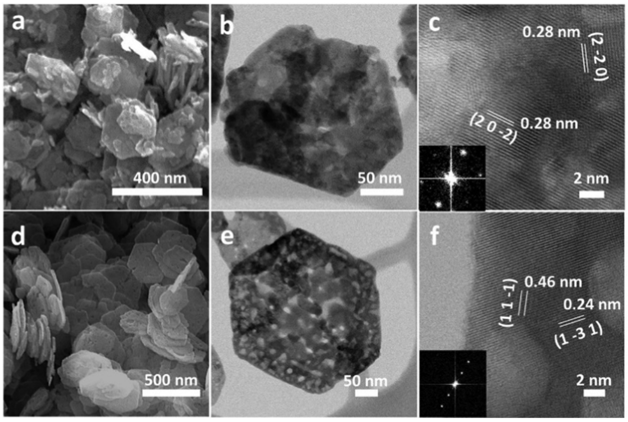

Fig. 1 (a) SEM, (b) STEM and (c) high-resolution STEM for 111-$NiCo_2O_4$-400 (inset: corresponding FFT pattern), (d) SEM, (e) STEM and (f) high-resolution STEM for 112-$NiCo_2O_4$-400 (inset: corresponding FFT pattern).

atomic size of Ni relative to Co in $NiCo_2O_4$, the metal–oxygen bond lengths are uneven within the structure making it thermal unstable. Consequently, spinel $NiCo_2O_4$ has been reported to decompose at around 400 °C resulting in the segregation of NiO from the structure.[3,23] The results obtained here attest for the higher thermal stability of 112-$NiCo_2O_4$ compared with 111-$NiCo_2O_4$. This could be attributed to the surface atomic arrangement in the high-index-faceted 112-$NiCo_2O_4$ that enhances its structural stability even at high temperatures.[26]

Scanning electron microscope (SEM) images in Fig. 1a and d show thin hexagonal nanoplate morphology of size *ca.* 200–350 nm for 111-$NiCo_2O_4$-400 and 300–400 nm for 112-$NiCo_2O_4$-400. Some small differences exist between the two samples such as the presence of small nanoparticles in 111-$NiCo_2O_4$-400 and the presence of a few through holes on the surfaces of 112-$NiCo_2O_4$-400 but we do not expect these minor variances to affect the overall CH_4 oxidation rates. Transmission electron microscopy (TEM) images in Fig. 1b and e show that both 111-$NiCo_2O_4$-400 and 112-$NiCo_2O_4$-400 have thin hexagonal nanoplate morphology. From the high-resolution Scanning transmission electron microscope (STEM) image of 111-$NiCo_2O_4$-400 in Fig. 1c, the visible planes are (2−20) and (20−2), both with lattice distance of 0.28 nm as confirmed by the Fast Fourier Transform (FFT) pattern (inset of Fig. 1c) and perpendicular to the {111} exposed facet according to the Weiss zone law.[41] Similarly in Fig. 1f, the {112} exposed facet is dominant in 112-$NiCo_2O_4$-400 which is normal to the (11−1) and (1−31) planes with lattice distances of 0.46 nm and 0.24 nm, respectively and in accordance with FFT pattern (inset of Fig. 1f). These results confirm that {111} and {112} are the dominant exposed facets on the surface of 111-$NiCo_2O_4$-400 and 112-$NiCo_2O_4$-400, respectively. From N_2 adsorption isotherms (Fig. S3, ESI†), it was evaluated that both samples had a similar Brunauer, Emmett and Teller (BET) specific surface areas with 38 $m^2\ g^{-1}$ for 111-$NiCo_2O_4$-400 and 37 $m^2\ g^{-1}$ for 112-$NiCo_2O_4$-400. These initial results confirm that the basic textural parameters of both samples (particles sizes, morphologies and surface areas) are comparable and therefore ideal for studying the effect of crystal exposed facet as a predominant variable for the catalytic oxidation of CH_4.

Hydrogen temperature-programmed-reduction (H_2-TPR) results in Fig. 2a reveal two reduction peaks for both samples. The first smaller peak is attributed to the reduction of M^{3+} cations to M^{2+} (M being the sum of Ni and Co atoms) while the second larger peak is due to the complete reduction of M^{2+} to M^0.[3] It was theoretically shown that M^{3+} species adsorb and activate the hydrocarbon molecules to be subsequently reduced to M^{2+} species during the oxidation reaction due to the donation of adjacent lattice oxygen atoms.[5,6] Hence, comparing the first peak temperatures for both samples, M^{3+} species in 112-$NiCo_2O_4$-400 can be more easily reduced (228.6 °C) than in 111-$NiCo_2O_4$-400 (261.2 °C). Good reducibility or the ability to give away lattice oxygen atoms is a vital characteristic for metal oxide catalysts used in oxidation reactions. Furthermore, by calculating and comparing the areas under the peaks, it can be determined that 112-$NiCo_2O_4$ had slightly higher amount of M^{3+} at 58% compared to 53% for 111-$NiCo_2O_4$-400. The CH_4 consumption and CO_2 evolved during methane temperature-programmed-reduction (CH_4-TPR) are shown in Fig. 2b. The CO_2 produced is a result of the reaction of the adsorbed CH_4 with lattice oxygen from the $NiCo_2O_4$ surface. The reduction peaks are attributed to the reduction process of M^{3+} to M^{2+}. [13] Water was also detected while negligible CO or H_2 occurred during this time (see Fig. S4 and S5 in the ESI† for more details). The CH_4 consumption peaks centred at 452 °C and 469 °C, closely correspond to the CO_2 evolution peaks centred at 446 °C and 466 °C for 112-$NiCo_2O_4$-400 and 111-$NiCo_2O_4$-400, respectively. Additionally, the ratio of the areas under the CO_2 formation peaks divulge that 20% more CO_2 was formed on 112-$NiCo_2O_4$-400 relative to 111-$NiCo_2O_4$-400. The lower reduction temperature of the 112-$NiCo_2O_4$ sample from the CH_4-TPR results may be due to the atomic arrangement on the 112 surface which facilitates CH_4 adsorption, activation and oxidation (as confirmed by DFT later). It is noticed that the

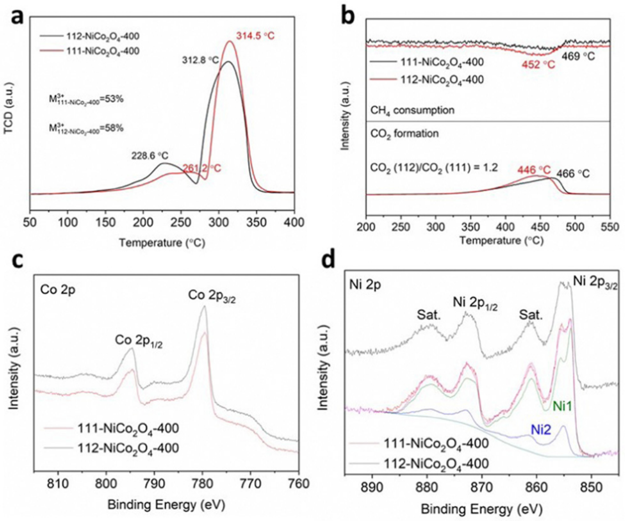

Fig. 2 (a) H_2-TPR, (b) CH_4-TPR, high-resolution XPS of (c) Co 2p and (d) Ni 2p for 111-$NiCo_2O_4$-400 and 112-$NiCo_2O_4$-400. A representative Ni 2p peak-fit using NiO (Ni1) and $Ni(OH)_2$ (Ni2) model spectra is shown for 111-$NiCo_2O_4$-400. See text for details.

amount of CO_2 generated (20% more for 112-$NiCo_2O_4$-400 compared with 111-$NiCo_2O_4$-400) does not correspond to the amounts of M^{3+} as suggested by the H_2-TPR profiles in the respective samples. This could be due to: (1) not all the M^{3+} species act as active sites or (2) different atomic arrangement on the differently exposed crystal facet, which creates a more active pathway for CH_4 oxidation reaction (as revealed later in the DFT calculation section) on the 112-$NiCo_2O_4$ sample. Nevertheless, the CH_4-TPR findings are in line with the H_2-TPR results indicating 112-$NiCo_2O_4$-400 as a more active catalyst than 111-$NiCo_2O_4$-400.

X-ray photoelectron spectroscopy (XPS) analysis of transition metal oxides is not a trivial exercise because the relevant metal 2p photoelectron signals are very complex, and different oxidation states cannot easily be determined, let alone quantified. Herein we mainly rely on the important studies published over the last 10–15 years to extract reliable and meaningful information about the nature of the Co and Ni species in the $NiCo_2O_4$ samples.[42–45] The Co 2p spectra for both 111-$NiCo_2O_4$-400 and 112-$NiCo_2O_4$-400 in Fig. 2c are similar and exhibit relatively narrow peak widths with flat, weak satellite structures. These features are characteristic to the presence of both Co^{3+} and Co^{2+}, with predominantly the higher oxidation state specie, in a spinel lattice.[42] Nevertheless, the quantification of all species is very difficult, not only because of the complex peak shape of the Co 2p doublet but also because of its significant overlap with both Co and Ni Auger peaks. An attempt at identifying and quantifying the two different oxidation states would be associated with large uncertainties and, therefore, be unreliable. The Ni 2p spectra for both samples are presented in Fig. 2d. They clearly display the characteristics of NiO, *i.e.*, a sharp intense peak at around 853.7 eV, a broader, weaker peak about 2 eV above the first peak, and a strong loss/satellite structure between 860 and 862 eV.[43–45] However, compared to the sharp low binding energy (BE) peak, the second peak at 855–856 eV is more intense as what would be observed in a pure NiO sample. This points to the possible presence of some $Ni(OH)_2$ which has been shown to be inherently present as an impurity in the form of a thin layer over synthesised NiO samples following exposure to ambient atmosphere.[43,44] Furthermore, the intense loss/satellites features indicate that the oxidation state of Ni is mainly 2+, *i.e.*, it is most probably present as NiO and $Ni(OH)_2$ rather than NiOOH.[43,44] Previous studies[39,40] have shown that the Ni is mostly present inside NiO_6 octahedral cells in the spinel structure of $NiCo_2O_4$ and this is depicted in Fig. S6a (ESI†). Similarly, the NiO crystal structure is an arrangement of NiO_6 octahedral cells, as shown in Fig. S6b (ESI†). Therefore, the Ni 2p spectra of both 111-$NiCo_2O_4$-400 and 112-$NiCo_2O_4$-400 samples are consistent with the NiO_6 octahedral cells present in the spinel $NiCo_2O_4$ structure. The O 1s spectra of both samples are similar and presented in Fig. S7 (ESI†). The C 1s spectra of the samples were used to determine the contribution to the total O 1s signal by organic carbon (see Fig. S8 for more details, ESI†). The compositions (atomic concentrations) of the samples are shown in Table S1 (ESI†). The measured Ni/Co atomic ratios are 1.0 and 0.7 for 111-$NiCo_2O_4$-400 and 112-$NiCo_2O_4$-400, respectively, deviating significantly from the stoichiometric value of 0.5. This can be attributed to the surface chemical arrangement being quite different from the bulk, noting that the XPS sampling depth is of the order of just a few nm. The Ni 2p spectra for both samples could be fitted reasonably well using model spectra derived from NiO and $Ni(OH)_2$ reference compounds (components Ni1 and Ni2, Fig. 2d). The ratio of NiO/$Ni(OH)_2$ for 111-$NiCo_2O_4$-400 was higher at 5.5 compared to 3.2 for 112-$NiCo_2O_4$-400, implying that more NiO_6 cells are present on the surface of 111-$NiCo_2O_4$-400. Due to the thermal instability of the spinel $NiCo_2O_4$ structure, at high temperatures, we surmise that the NiO_6 octahedral cells tend to detach from the structure and migrate towards the surface of the catalyst where they can assemble into NiO fine nanocrystals, which then get coated with a thin $Ni(OH)_2$ layer once exposed to ambient air.[22,23] This is consistent with the observed variation of the NiO/$Ni(OH)_2$ ratio in Table S1 (ESI†). Indeed, it was found that the samples calcined at a higher temperature of 450 °C present a surface enriched in NiO relative to the samples calcined at 400 °C. Furthermore, this ratio is higher for 111-$NiCo_2O_4$-450 compared to 112-$NiCo_2O_4$-450, which is in line with our XRD observations (Fig. S1 and S2, ESI†) that suggest that the sample with {112} exposed facets have a better thermal stability than the one with {111} exposed facets.

Comparison of 111 *vs.* 112 – DFT and experimental validation

An earlier density functional theory (DFT) study on $NiCo_2O_4$ with {110} exposed facets revealed that the most active site for CH_4 adsorption and activation was Ni^{3+} situated in octahedral cells within the spinel lattice and that CH_4 oxidation could follow two reaction pathways.[5] In pathway 1, only Ni^{3+} acted as the active site while in pathway 2, both Ni^{3+} and Co^{3+} were considered as active sites. Both pathways shared steps in common for CH_4 adsorption and its dissociation into $^*CH_3$ and $^*H$. In our work according to DFT modelling, 2 analogous pathways were energetically feasible on the surfaces of 111-$NiCo_2O_4$ and 112-$NiCo_2O_4$ for complete CH_4 oxidation. Firstly, it needs to be specified that the {111} facet exposes only Ni atoms on its surface while the {112} facet exposes both Ni and Co atoms (see Fig. S9 for DFT generated model representations, ESI†). The types of exposed metal atoms as well as their geometrical arrangement will clearly affect the adsorption of CH_4 as well as its reaction mechanism towards complete oxidation. For pathway 1 on 111-$NiCo_2O_4$, only the Ni atom in the octahedral cell was the active site while in pathway 2 an O atom associated with a neighbouring Co atom also participated in the reaction mechanism. Regarding the 112-$NiCo_2O_4$ surface, pathway 1 involved one Ni and one Co atom in the reaction route while pathway 2 entailed two Ni atoms and one Co atom as participatory active sites. Fig. 3 displays the Gibbs free energy profiles of both pathways on the 112-$NiCo_2O_4$ surface as well as some representative molecular conformations derived from DFT modelling. The corresponding results for 111-$NiCo_2O_4$ are given in Fig. S10 (ESI†). Simplified diagrams of the detailed interactions of CH_4 and intermediates on the catalysts' surfaces are presented in Fig. S11–S14 (ESI†).

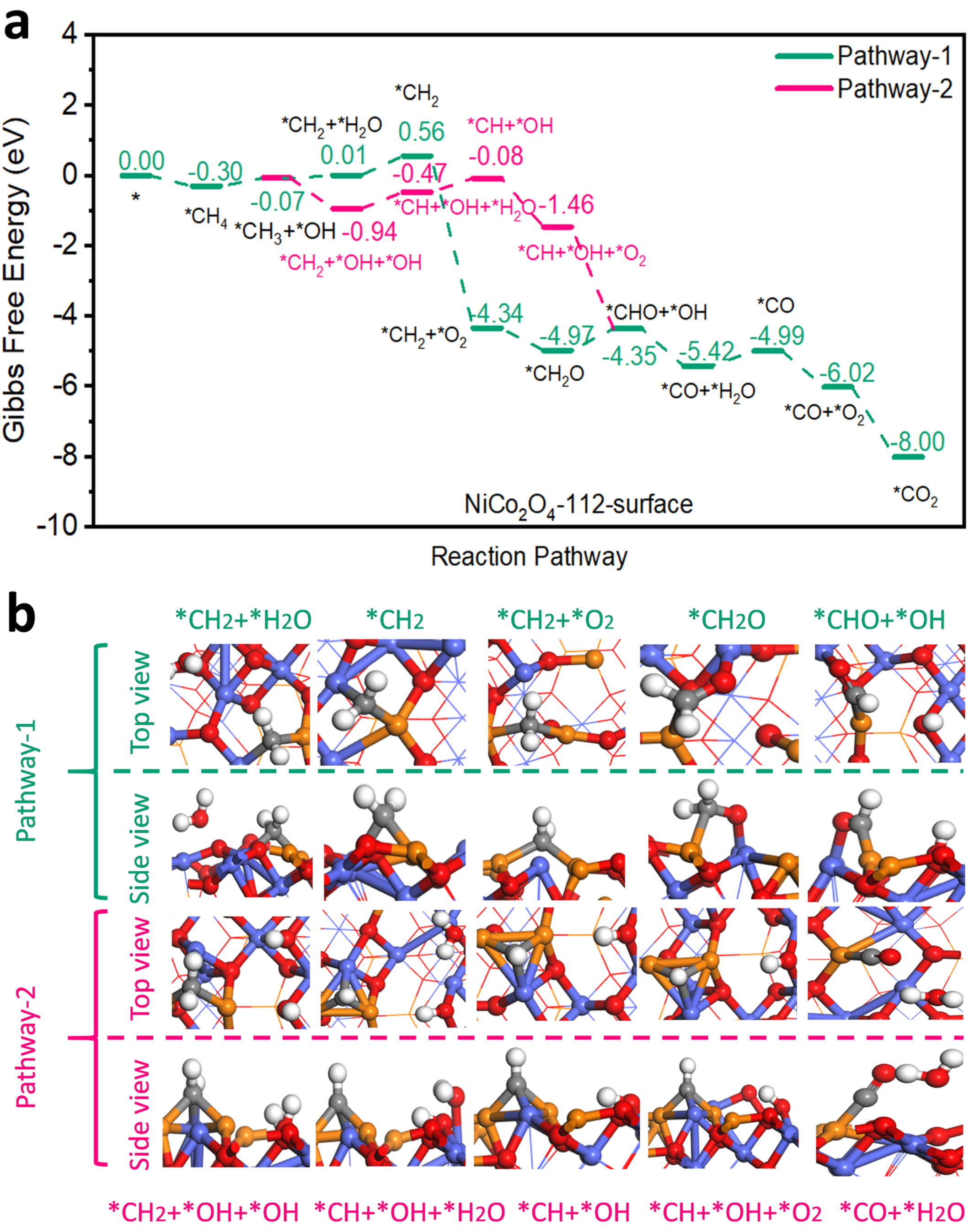

Fig. 3 (a) Gibbs free energy diagram showing pathways and (b) selected molecular conformations for CH_4 oxidation on the 112-$NiCo_2O_4$ surface.

The complete oxidation of CH_4 on both $NiCo_2O_4$ surfaces consisted of 11 elementary steps. The first step involving the adsorption of CH_4 on Ni active sites, exhibited a stronger binding energy of −0.30 eV on 112-$NiCo_2O_4$ compared to −0.19 eV on 111-$NiCo_2O_4$. This means that the 112-$NiCo_2O_4$ surface had a relatively better affinity for CH_4 capture and adsorption. Following the initial adsorption step, CH_4 had to overcome an activation barrier to dissociate into adsorbed $*CH_3$ and *H species. Thereafter sequential oxidation of $*CH_3$ to, $*CH_2$, *CHO, *CO and finally $*CO_2$ occurred by reaction with lattice surface oxygen. In detail, taking the 112-surface and pathway 1 as example, a H atom migrates from the $*CH_3$ to produce $*CH_2$ species with one water molecule released to the atmosphere. DFT calculated results suggest that an uphill free energy change is required for this step. However, for pathway 2, there is interaction between the $*CH_3$ and the closest Co atom, which facilitates the migration of a H atom from $*CH_3$ to the lattice O in the vicinity of the Co atom. As a result, the free energy change strongly decreases to −0.87 eV. Hence pathway 2 is much more favourable for CH_4 oxidation on the 112-surface. After the formation of $*CH_2$ + *OH + *OH, the $*CH_2$ can dissociate into *CH, releasing one H atom to the lattice O of the nearby Co atom to form a water molecule, with the free energy change slightly increasing for this step. Then the first O_2 molecule can be adsorbed into the generated oxygen vacancy with a significantly downhill free energy change. The adsorbed oxygen reacts with the *CH species to produce *CHO and *OH intermediates. The next step is the formation of CO molecule on the Ni active site. After that, another O_2 molecule that gets adsorbed into an oxygen vacancy site reacts with the *CO to produce *CO_2 which eventually desorbs from the active site and ends the complete oxidation cycle on 112-$NiCo_2O_4$. From Fig. S10a (ESI†), pathway 1 is the favoured route for CH_4 oxidation on 111-$NiCo_2O_4$ since two uphill free energy changes are involved with a total energy requirement of 2.78 eV compared with three uphill free energy steps in pathway 2 having a total energy demand of 3.37 eV.

For 112-$NiCo_2O_4$ the potential limiting step for pathway 1 is the formation of *CHO with an energy requirement of 0.62 eV while for pathway 2, the potential limiting step is the formation of *CH with an energy requirement of 0.47 eV. In the case of 111-$NiCo_2O_4$, the potential limiting step for pathway 1 is the formation of *CH_2 with an energy barrier of 1.61 eV while for pathway 2, the potential limiting step is the formation of *CH with an energy requirement of 1.38 eV. For both pathways, these intermediate reaction energy barriers were much larger on the 111-surface compared to the 112-surface. Consequently, CH_4 oxidation should theoretically be favoured on the 112-surface compared with the 111-surface.

We performed CH_4 catalytic oxidation light-off experiments to verify this. We used the samples calcined at 400 °C due to their comparable physical and textural parameters (see XRD, SEM, TEM and N_2 adsorption results discussed earlier). The CH_4 catalytic oxidation experiments were carried out up to a temperature of 500 °C for the sake of completion of the light-off curves (Fig. 4a). However due to the thermal instability of the samples at temperatures higher than their calcination temperatures, we compared the data up to a catalytic oxidation temperature of 400 °C (Fig. S15, ESI†). From Fig. S15 (ESI†), 112-$NiCo_2O_4$ outperforms 111-$NiCo_2O_4$ under both dry and humid conditions over the whole temperature range investigated, achieving 80% and 65% methane conversion at 400 °C, respectively. These findings are in line with our DFT simulation results.

Effect of humidity

The presence of water vapour in the feed reduces the catalytic activity of both samples. To explain this, DFT simulations were carried out to calculate the adsorption energies and activation barriers of water on both surfaces (Table S2, ESI†). Interestingly, computer modelling indicated that water could be adsorbed on both Co and Ni atoms on the 112-surface, with the Co sites strongly preferred with an adsorption energy of −1.59 eV. Interaction of water molecules with the Ni site is also feasible due to an exothermic adsorption energy of −0.52 eV. Conversely, water could only adsorb on the Ni sites on the 111-surface with an adsorption energy of −0.94 eV. These adsorption energies are much more exothermic than those for CH_4, meaning that water molecules will preferentially adsorb on the active sites instead of CH_4 when the feed is humid. Furthermore,

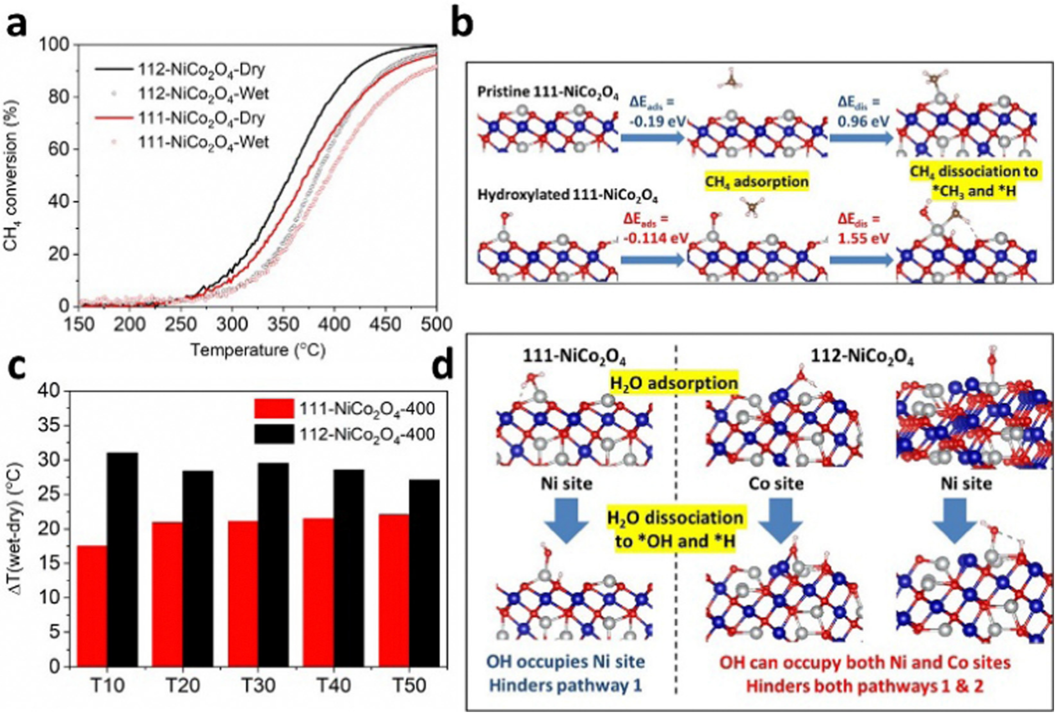

Fig. 4 (a) Light-off curves for CH_4 oxidation (3.2% water vapor concentration under humid conditions), (b) DFT simulations comparing the adsorption and dissociation of methane on pristine and hydroxylated 111-$NiCo_2O_4$, (c) the temperature difference between wet and dry conditions at several T_x points for 111-$NiCo_2O_4$-400 and 112-$NiCo_2O_4$-400 and (d) water adsorption and dissociation on 111-$NiCo_2O_4$ and 112-$NiCo_2O_4$ active sites.

the energy required to dissociate a water molecule into adsorbed *OH (on the active metal sites) and *H (on the neighbouring lattice O sites) is 0.84 eV on the 112-surface and 0.66 eV on the 111-surface, resulting in heavily hydroxylated $NiCo_2O_4$ surfaces. These energy requirements are less positive than the corresponding energies required for CH_4 (Table S3, ESI†) and suggest that water adsorption and dissociation on the spinel $NiCo_2O_4$ active sites are feasible and indeed thermodynamically preferred to CH_4 adsorption and activation. We performed further DFT calculations to determine how CH_4 is adsorbed and activated on hydroxylated 112-$NiCo_2O_4$ and 111-$NiCo_2O_4$ surfaces. From molecular modelling, a stable conformation of the hydroxyl molecule could be maintained on the 112-$NiCo_2O_4$ surface when the O from OH is bonded to one Ni and one Co atoms. Methane can then adsorb onto the hydroxylated Ni atoms with an adsorption energy of −0.14 eV and then dissociate into $*CH_3$ and *H species with a high energy requirement of 1.38 eV. On the 111-$NiCo_2O_4$ surface, the O atom from the hydroxyl is bonded to one Ni atom. The corresponding adsorption and dissociation energies of CH_4 on the hydroxylated Ni atoms is calculated as −0.11 eV and 1.55 eV, respectively. Fig. 4b and Fig. S16 (ESI†) compares the adsorption and dissociation of CH_4 on both pristine and hydroxylated surfaces of 111-$NiCo_2O_4$ and 112-$NiCo_2O_4$, respectively. The results show that CH_4 adsorption and dissociation is much harder on hydroxylated $NiCo_2O_4$ surfaces compared to the pristine surfaces. Hence, the presence of water vapour in the feed has a dual negative effect upon the activity of the catalyst. Firstly, H_2O adsorption and activation are thermodynamically preferred to CH_4 onto the active sites. This creates a hydroxylated surface which reduces the number of active sites available for CH_4 adsorption and activation. Secondly, CH_4 adsorption and activation is energetically harder on the hydroxylated surfaces relative to the pristine surfaces. These findings explain our experimental results as to how the presence of humidity in the feed negatively impacts the active sites on the spinel surface and reduces the catalytic activity towards methane oxidation.

Although the 112-$NiCo_2O_4$ sample performs better than 111-$NiCo_2O_4$ under humid conditions, it appears that relative to its activity under dry conditions the 111-$NiCo_2O_4$ sample is more resistant to water vapour than 112-$NiCo_2O_4$. This is evident in Fig. 4c, where we compare the temperature difference between wet and dry conditions at different T_x (x = 10, 20, 30, 40, 50 and 60, where for example T_{10} is the temperature at which 10% methane conversion occurs). This temperature difference is consistently larger for the 112-$NiCo_2O_4$ sample over the temperature range of interest. Fig. 4d shows the molecular arrangements for H_2O adsorption and dissociation on both 111-$NiCo_2O_4$ and 112-$NiCo_2O_4$, as determined from DFT simulations. The favoured adsorption and dissociation of water on both Ni and Co sites on 112-$NiCo_2O_4$ could hinder both pathways 1 and 2 for the methane oxidation reaction (since both Ni and Co sites are involved in the reaction mechanism, as mentioned in the DFT modelling section). However, since water adsorbs on the Ni sites on 111-$NiCo_2O_4$ (as only Ni sites are exposed to the reactants, see DFT section), this may hinder pathway 1 of the reaction but it may be possible that the methane oxidation reaction shifts to the alternative pathway 2 on this surface during reaction under humid conditions. On the 111-$NiCo_2O_4$ surface, some H atoms from dissociated H_2O molecules will occupy the oxygen sites bonded to the Ni active sites, which may thwart the oxidation reaction. Therefore, the lattice O associated with a Co atom could alleviate this burden by participating in the oxidation reaction *via* pathway 2 (Fig. S12, ESI†). These reasons may explain why 111-$NiCo_2O_4$ is more resistant to water vapour than 112-$NiCo_2O_4$.

Interestingly, the results in this study reveal that different exposed crystal facets provide different sought-after properties for the catalytic oxidation of methane, *i.e.*, high activity and thermal stability on the {112} exposed facet of 112-$NiCo_2O_4$ and good water resistance/relative hydrophobicity on the {111} exposed facet of 111-$NiCo_2O_4$.

Stability tests

Preliminary stability tests were performed at 500 °C under humid conditions (3.2% water) over *ca.* 35 hours on 111-$NiCo_2O_4$ and 112-$NiCo_2O_4$ samples calcined at 450 °C (Fig. 5a). As expected, 112-$NiCo_2O_4$-450 shows better activity and stability with initial methane conversion of 97.6% and a final conversion of 90.4%, hence a 7.2% activity loss after 35 h reaction. Comparatively, 111-$NiCo_2O_4$-450 starts at 89.9% methane conversion but loses 11.2% activity after 35 h reaction, reaching only 78.8% conversion. To estimate the relative degree of NiO segregation from the spent samples, we calculated the ratio R of the peak heights at 50.756° with Miller index (012) for NiO to the peak height at 52.332° with Miller index (004) for $NiCo_2O_4$ from the XRD patterns of the fresh and spent samples in Fig. S17 and S18 (ESI†). The value of R is 2.2 for spent 111-$NiCo_2O_4$-450 compared with 1.6 for spent 112-$NiCo_2O_4$-450. This means that more NiO was segregated from the bulk spinel structure in the spent 111-$NiCo_2O_4$-450. This is expected as we earlier showed that 112-$NiCo_2O_4$ was more thermally stable than 111-$NiCo_2O_4$. XPS provides the relevant surface data of the tested samples. Table S1 (ESI†) presents a comparison of the NiO/$Ni(OH)_2$ ratios based on XPS analysis of the fresh and spent samples. The appropriately peak-fitted Ni 2p spectra for fresh and spent 111-$NiCo_2O_4$-450 and 112-$NiCo_2O_4$-450 are shown in Fig. 5b. Please note that we observed hardly any difference between the Co 2p spectra for fresh and spent samples, indicating that Co did not undergo any significant changes during testing (see Fig. S19, ESI†). However, a large increase in the NiO/$Ni(OH)_2$ ratios for both after-test samples was determined when compared to the fresh samples (Table S1, ESI†), consistent with the detachment of the NiO_6 cells from the spinel structure, followed by their migration towards the catalyst surface and assembling into NiO nanocrystals. Nevertheless, from Table S1 (ESI†), while the Ni/Co ratios for both spent samples are similar, it is interesting to see that the NiO/$Ni(OH)_2$ values for both spent samples are also comparable at *ca.* 14. This may be attributed to the high reaction temperature of 500 °C as well as long reaction time under humid conditions which are severe conditions for the integrity of the catalyst structure to be maintained. Hence, XPS results indicate

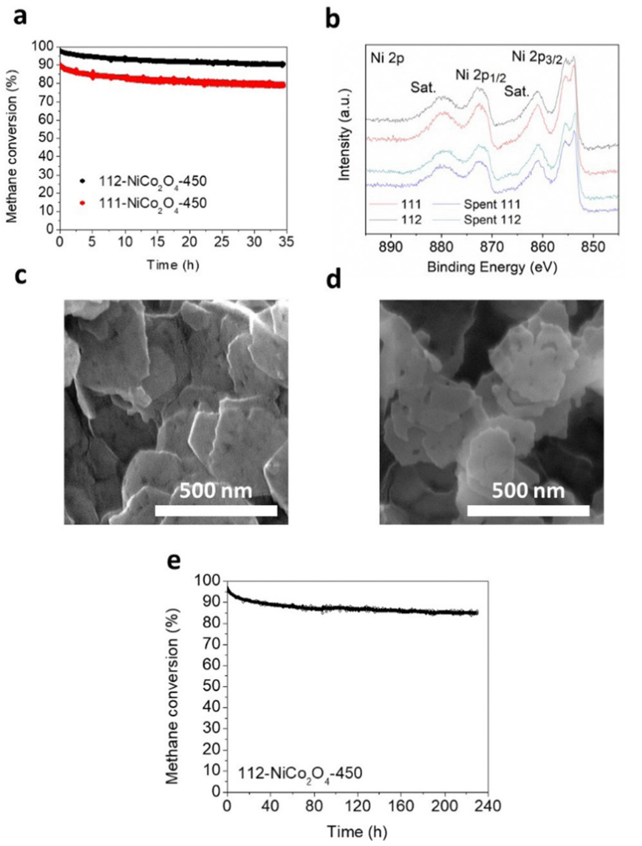

Fig. 5 (a) Preliminary stability rest comparing 111-NiCo$_2$O$_4$-450 and 112-NiCo$_2$O$_4$-450 at 3.2% water vapor concentration and a reaction temperature of 500 °C, (b) high-resolution XPS Ni 2p spectra for fresh and spent 111-NiCo$_2$O$_4$-450 and 112-NiCo$_2$O$_4$-450, SEM image of (c) 112-NiCo$_2$O$_4$-450 and (d) spent 112-NiCo$_2$O$_4$-450 and (e) long-term stability over 230 h for the catalytic oxidation of CH$_4$ using 112-NiCo$_2$O$_4$-450 at 3.2% water vapor concentration and a reaction temperature of 500 °C.

similar degrees of atomic rearrangements occurring on the surfaces of spent 111-NiCo$_2$O$_4$-450 and 112-NiCo$_2$O$_4$-450 although XRD results showed more NiO being segregated within the bulk of 111-NiCo$_2$O$_4$-450, which can be attributed to the lower thermal stability of NiCo$_2$O$_4$ with {111} exposed facets. Nevertheless, the comparatively similar surface NiO/Ni(OH)$_2$ as well as Ni/Co ratios on the spent samples further confirm our findings from Fig. 4a, *i.e.*, the {112} exposed facet is more active than the {111} exposed facet in NiCo$_2$O$_4$ for methane oxidation reaction, (since despite the harsh conditions used, it can be assumed that some of the exposed crystal facets initially present in the pristine samples are retained during stability testing). The SEM image in Fig. 5c show the thin hexagonal morphology of fresh 112-NiCo$_2$O$_4$-450. The structure is still somehow preserved in the spent sample (Fig. 5d) although a certain degree of sintering as well as edge-etching are observed on the particles. On the other hand, spent 111-NiCo$_2$O$_4$-450 shows a relatively higher level of particles sintering (Fig. S20, ESI†). Hence an overall better thermal structural stability is evident with 112-NiCo$_2$O$_4$-450 when compared with 111-NiCo$_2$O$_4$-450.

Long term stability test was performed on 112-NiCo$_2$O$_4$-450 for *ca.* 230 h (Fig. 5d) at 500 °C under humid conditions (3.2% water). It can be seen that after the relatively large activity loss from 97.1% to 88.3% in the first 50 h of reaction time, good stability is maintained such that the catalyst still retains 85.7% activity after 230 h reaction. Table S4 (ESI†) compares the activity of the catalyst in this work with other similar types of catalysts from previous publications. The impressive maintenance in activity can be credited to the high structural stability and activity of the NiCo$_2$O$_4$ spinel catalyst with {112} exposed facets.

Conclusions

The use of spinel NiCo$_2$O$_4$ materials for catalytic oxidation reaction at high temperatures has been impaired mostly due to its low thermal stability. The stability and activity of NiCo$_2$O$_4$ for methane oxidation is largely dependent on the atomic arrangement at the catalysts' surface. We demonstrate that NiCo$_2$O$_4$ with {112} exposed facets is more stable and active than its counterpart with {111} exposed facets. DFT simulations indicate that the reaction mechanism for methane oxidation is less challenging on 112-NiCo$_2$O$_4$ as it offers less energetically intensive alternate pathways for the oxidation of reaction intermediates as opposed to 111-NiCo$_2$O$_4$. In addition, 111-NiCo$_2$O$_4$ had the better water resistance of the two samples. This is because different exposed facets could also affect the way that water molecules present in the feed interact with the surface-active sites and therefore affect the activity of the material under humid conditions. The experimental and theoretical findings in this work would pave the way for crystal facet engineering (in conjunction with other strategies such as doping, compositing and hierarchical structure design) as a powerful, elegant and facile method towards the development of abundant metal oxide catalyst materials with tuneable activity, stability and hydrophobicity for the complete oxidation of dilute methane. These low-cost and high-performance catalysts are highly demanded for mitigating fugitive methane emissions in resources and energy sectors such as coal mining, natural gas industry, natural gas engines, *etc.*

Conflicts of interest

There are no conflicts of interest to declare.

Acknowledgements

This work was funded by CSIRO and the Australian Coal Industry's Research Program (ACARP). Partially supported by the National Key R&D Program of China (no. 2022YFA1504500, 2021YFA1502804).

References

1 I. Karakurt, G. Aydin and K. Aydiner, *Renewable Sustainable Energy Rev.*, 2011, **15**, 1042–1049.
2 L. He, Y. Fan, J. Bellettre, J. Yue and L. Luo, *Renewable Sustainable Energy Rev.*, 2020, **119**, 109589.

3 T. Lim, S. Cho, H. Yang, M. Engelhard and D. Kim, *Appl. Catal., A*, 2015, **505**, 62–69.

4 L. Hu, Q. Peng and Y. Li, *J. Am. Chem. Soc.*, 2008, **130**, 16136–16137.

5 F. Tao, J. Shan, L. Nguyen, Z. Wang, S. Zhang, L. Zhang, Z. Wu, W. Huang, S. Zeng and P. Hu, *Nat. Commun.*, 2015, **6**, 7798.

6 X. Xie, Y. Li, Z. Liu, M. Haruta and W. Shen, *Nature*, 2009, **458**, 746–749.

7 S. Rong, P. Zhang, F. Liu and Y. Yang, *ACS Catal.*, 2018, **8**, 3435–3446.

8 J. Huang, R. Fang, Y. Sun, J. Li and F. Dong, *Chemosphere*, 2021, **263**, 128103.

9 J. Niu, H. Liu, Y. Zhang, X. Wang, J. Han, Z. Yue and E. Duan, *Chemosphere*, 2020, **259**, 127427.

10 Y. Jian, M. Tian, C. He, J. Xiong, Z. Jiang, H. Jin, L. Zheng, R. Albilali and J. Shi, *Appl. Catal., B*, 2021, **283**, 119657.

11 H. Liu, X. Li, Q. Dai, H. Zhao, G. Chai, Y. Guo, Y. Guo, L. Wang and W. Zhan, *Appl. Catal., B*, 2021, **282**, 119577.

12 D. Jiang, K. Khivantsev and Y. Wang, *ACS Catal.*, 2020, **10**, 14304–14314.

13 L. Hu, Q. Peng and Y. Li, *J. Am. Chem. Soc.*, 2008, **130**, 16136–16137.

14 S. Zhao, T. Li, J. Lin, P. Wu, Y. Li, A. Li, T. Chen, Y. Zhao, G. Chen, L. Yang, Y. Meng, X. Jin, Y. Qiu and D. Ye, *Chem. Eng. J.*, 2021, **420**, 130448.

15 Y. Zheng, Y. Liu, H. Zhou, W. Huang and Z. Pu, *J. Alloys Compd.*, 2018, **734**, 112–120.

16 Z. Fei, S. He, L. Li, W. Ji and C. Au, *Chem. Commun.*, 2012, **48**, 853–855.

17 Q. Kong, Y. Yin, B. Xue, Y. Jin, W. Feng, Z.-G. Chen, S. Su and C. Sun, *Beilstein J. Nanotechnol.*, 2018, **9**, 2526–2532.

18 Y. Dai, V. P. Kumar, C. Zhu, H. Wang, K. J. Smith, M. O. Wolf and M. J. MacLachlan, *Adv. Funct. Mater.*, 2019, **29**, 1807519.

19 J. Dou, Y. Tang, L. Nie, C. Andolina, X. Zhang, S. House, Y. Li, J. Yang and F. Tao, *Catal. Today*, 2018, **311**, 48–55.

20 Y. Zhang, Z. Qin, G. Wang, H. Zhu, M. Dong, S. Li, Z. Wu, Z. Li, Z. Wu, J. Zhang, T. Hu, W. Fan and J. Wang, *Appl. Catal., B*, 2013, **129**, 172–181.

21 X. Huang, J. Li, J. Wang, Z. Li and J. Xu, *Front. Chem. Sci. Eng.*, 2020, **14**, 534–545.

22 M. Cabo, E. Pellicer, E. Rossinyol, O. Castel, S. Surinach and M. Baro, *Cryst. Growth Des.*, 2009, **9**, 4814–4821.

23 S. Verma, H. Joshi, T. Jagadale, A. Chawla, R. Chandra and S. Ogale, *J. Phys. Chem. C*, 2008, **112**, 15106–15112.

24 A. Datye and M. Votsmeier, *Nat. Mater.*, 2021, **20**, 1049–1059.

25 D. Qiao, G. Lu, Y. Guo, Y. Wang and Y. Guo, *J. Rare Earths*, 2010, **28**, 742–746.

26 C. Xiao, B. Lu, P. Xue, N. Tian, Z. Zhou, X. Lin, W. Lin and S. Sun, *Joule*, 2020, **4**, 2562–2598.

27 X. Han, G. He, Y. He, J. Zhang, X. Zheng, L. Li, C. Zhong, W. Hu, Y. Deng and T. Ma, *Adv. Energy Mater.*, 2018, **8**, 1702222.

28 C. Chang, K. Chen, Y. Hsieh, C. Chang and H. Tuan, *ACS Nano*, 2022, **16**, 1486–1501.

29 X. Gao and T. Zhang, *Sens. Actuators, B*, 2018, **277**, 604–633.

30 S. Wang, G. Liu and L. Wang, *Chem. Rev.*, 2019, **119**, 5192–5247.

31 L. Fang, Z. Jiang, H. Xu, L. Liu, Y. Guan, X. Gu and Y. Wang, *J. Catal.*, 2018, **357**, 238–246.

32 G. Liu, J. Yu, G. Lu and H. Cheng, *Chem. Commun.*, 2011, **47**, 6763–6783.

33 L. Ma, R. Ye, Y. Huang, T. Reina, X. Wang, C. Li, X. Li Zhang, M. Fan, R. Zhang and J. Liu, *Chem. Eng. J.*, 2022, **446**, 137031.

34 C. Yang, C. Pei, R. Luo, S. Liu, Y. Wang, Z. Wang, Z. Zhao and J. Gong, *J. Am. Chem. Soc.*, 2020, **142**, 19523–19531.

35 Q. Kuang, X. Wang, Z. Jiang, Z. Xie and L. Zheng, *Acc. Chem. Res.*, 2014, **47**, 308–318.

36 S. Devaguptapu, S. Hwang, S. Karakalos, S. Zhao, S. Gupta, D. Su, H. Xu and G. Wu, *ACS Appl. Mater. Interfaces*, 2017, **9**, 44567–44578.

37 J. Bae, D. Shin, H. Jeong, C. Choe, Y. Choi, J. Han and H. Lee, *ACS Catal.*, 2021, **11**, 11066–11074.

38 Z. Xu, Y. Zhang, L. Qin, Q. Meng, Z. Xue, L. Qiu, G. Zhang, X. Guo and Q. Li, *Small*, 2020, **16**, 2002071.

39 M. Iliev, P. Silwal, B. Loukya, R. Datta, D. Kim, N. Todorov, N. Pachauri and A. Gupta, *J. Appl. Phys.*, 2013, **114**, 033514.

40 J. Marco, J. Gancedo, M. Gracia, J. Gautier, E. Rios, H. Palmer, C. Greaves and F. Berry, *J. Mater. Chem.*, 2001, **11**, 3087–3093.

41 S. Sun, X. Zhang, J. Cui and S. Liang, *Nanoscale*, 2020, **12**, 16657–16677.

42 M. Biesinger, B. Payne, A. Grosvenor, L. Lau, A. Gerson and R. Smart, *Appl. Surf. Sci.*, 2011, **257**, 2717–2730.

43 M. Biesinger, B. Payne, L. Lau, A. Gerson and R. Smart, *Surf. Interface Anal.*, 2009, **41**, 324–332.

44 A. Grosvenor, M. Biesinger, R. Smart and N. McIntyre, *Surf. Sci.*, 2006, **600**, 1771–1779.

45 M. Biesinger, L. Lau, A. Gerson and R. Smart, *Phys. Chem. Chem. Phys.*, 2012, **14**, 2434–2442.